

1 **Do surface lateral flows matter for data assimilation of soil moisture observations**  
2 **into hyperresolution land models?**

3 **Running title: HYPERRESOLUTION LAND DATA ASSIMILATION**

4 Yohei Sawada<sup>1</sup>,

5 <sup>1</sup> Meteorological Research Institute, Japan Meteorological Agency, Tsukuba, Japan

6 Corresponding author: Y. Sawada, Meteorological Research Institute, Japan  
7 Meteorological Agency, 1-1, Nagamine, Tsukuba, Japan, ysawada@mri-jma.go.jp

8  
9 This article is a non-peer reviewed preprint published at EarthArXiv.

10  
11 **Key Points:**

- 12 1. Surface lateral flows matter when soil moisture observations are assimilated into  
13 high-resolution integrated surface-groundwater land models.  
14 2. The efficiency of an ensemble Kalman filter to assimilate soil moisture observations  
15 depends on soil characteristics.

16  
17 **Keywords:** data assimilation, hyperresolution land model, soil moisture

18  
19 **Abstract**

20 Hyperresolution land modeling is expected to innovate the simulation of terrestrial water,  
21 energy, and carbon cycles. One of the major advantages of existing hyperresolution land  
22 models against conventional 1-dimensional land surface models is that surface and  
23 subsurface lateral water flows can be explicitly simulated. Despite a lot of efforts on  
24 assimilating hydrological observations into the hyperresolution integrated surface-  
25 groundwater land models, how and in what case topography-driven surface water flows  
26 matter for data assimilation of soil moisture observations has yet to be clarified. In this  
27 study, I perform a minimalist synthetic numerical experiment, in which shallow soil  
28 moisture observations are assimilated into an integrated surface-groundwater land model  
29 by the ensemble Kalman filter. Propagation of a model error due to surface lateral water  
30 flows is crucially important to adjust the unobserved model state and parameter variables  
31 by horizontally propagating the information of soil moisture observations. However, the  
32 non-Gaussianity of the model error induced by the nonlinear dynamics of topography-  
33 driven surface flows harms the performance of an ensemble Kalman filter and the  
34 efficiency of data assimilation strongly depends on soil characteristics. The new  
35 capability of data assimilation with the hyperresolution land models found in this study  
36 may improve the monitoring and prediction of flash floods caused by local severe rainfalls.

37

38

## 39 **1. Introduction**

40 Hyperresolution land modeling is expected to innovate the simulation of terrestrial water,  
41 energy, and carbon cycles, which is crucially important for meteorological, hydrological  
42 and ecological applications. While conventional land surface models (LSMs) assume that  
43 lateral water flows are negligible at a coarse resolution and solve vertical 1-dimensional  
44 Richards equation for the soil moisture simulation (e.g., Sellers et al. 1996; Lawrence et  
45 al. 2011), currently proposed hyperresolution land models, which can be applied at a finer  
46 resolution (<1km), explicitly consider surface and subsurface lateral water flows (e.g.,  
47 Maxwell and Miller 2005; Tian et al. 2012; Shrestha et al. 2014; Niu et al. 2014). Previous  
48 works indicated that a lateral transport of water plays important roles in terrestrial water  
49 and energy cycles (e.g., Maxwell and Condon 2016; Ji et al. 2017; Fang et al. 2017) and  
50 land-atmosphere interactions (e.g., Williams and Maxwell 2011; Keune et al. 2016).

51

52 Data assimilation has contributed to improving the performance of LSMs by fusing  
53 simulation and observation. The grand challenge of land data assimilation is to estimate  
54 unobservable variables from observations by propagating observations' information into  
55 model's high dimensional state and parameter space. In previous works on the  
56 conventional 1-D LSMs, many land data assimilation systems (LDASs) have been  
57 proposed to accurately estimate model's state and parameter variables, which cannot be  
58 directly observed, by assimilating satellite and in-situ observations. For example, the  
59 optimization of LSM's unknown parameters (e.g., hydraulic conductivity) has been  
60 implemented by assimilating remotely sensed microwave observations (e.g., Yang et al.  
61 2007; Yang et al. 2009; Bandara et al. 2014; Bandara et al. 2015; Sawada and Koike 2014;  
62 Han et al. 2014). Kumar et al. (2009) analyzed the simulated correlation between surface  
63 soil moisture and root-zone soil moisture to improve the simulation of root-zone soil  
64 moisture by assimilating remotely sensed surface soil moisture observations. Sawada et  
65 al. (2015) successfully improved the simulation of root-zone soil moisture by assimilating  
66 microwave brightness temperature observations which include the information of  
67 vegetation water content. Gravity Recovery and Climate Experiment total water storage  
68 observation has been intensively used to improve the simulation of groundwater and soil  
69 moisture (e.g., Li et al. 2012; Houborg et al. 2012). Improving the simulation of state  
70 variables such as soil moisture and biomass by LDASs has contributed to accurately  
71 estimating fluxes such as evapotranspiration (e.g. Martens et al. 2017) and CO<sub>2</sub> flux (e.g.,  
72 Verbeeck et al. 2011). However, in most of the studies on the conventional 1-D LDASs,

73 observations impacted state and parameter variables only in a single model's horizontal  
74 grid which is identical to the location of the observation. The assumption that the surface  
75 and subsurface water flows are restricted to vertical direction in LSMs makes it difficult  
76 to propagate observation's information horizontally, which limits the potential of land  
77 data assimilation to fully use land hydrological observations.

78

79 The hyperresolution land models, which explicitly solve surface and subsurface lateral  
80 flows, provide a unique opportunity to examine the potential of land data assimilation to  
81 propagate observation's information horizontally in a model space and efficiently use  
82 land hydrological observations. Previous works successfully applied Ensemble Kalman  
83 Filters (EnKF) to 3-D Richards' equation-based integrated surface-groundwater models.  
84 For example, Camporese et al. (2009) and Camporese et al. (2010) successfully  
85 assimilated the synthetic observations of surface pressure head and streamflow into the  
86 Catchment Hydrology (CATHY). Kurtz et al. (2016) coupled the Parallel Data  
87 Assimilation Framework (PDAF) (Nerger and Hiller 2013) with the Terrestrial System  
88 Modelling Framework (TerrSysMP) (Shrestha et al. 2014). The performance of  
89 TerrSysMP-PDAF to assimilate soil moisture observations was evaluated by a simple  
90 synthetic experiment (see also Zhang et al. (2018)).

91

92 Although the data assimilation of hydrological observations into the hyperresolution land  
93 models has been successfully implemented in the synthetic experiments, it is unclear how  
94 and in what case topography-driven surface lateral water flows matter for data  
95 assimilation of soil moisture observations. Previous studies on data assimilation with high  
96 resolution models mainly focused on assimilating groundwater observations (e.g., Ait-El-  
97 Fquih et al. 2016; Rasmussen et al. 2015; Hendricks-Franssen et al. 2008). There are some  
98 applications which focused on the observation of soil moisture and pressure head in  
99 shallow unsaturated soil layers. However, in those literatures, topography-driven surface  
100 flows have not been considered in the experiment (Kurtz et al. 2016) or the role of them  
101 in assimilating observations into the hyperresolution land models has not been  
102 quantitatively discussed (Camporese et al. 2010; Camporese et al. 2009). This study aims  
103 at clarifying if surface lateral flows matter for data assimilation of soil moisture  
104 observations into hyperresolution land models by a minimalist numerical experiment.

105

106

107

108

109

## 110 2. Methods

### 111 2.1. Model

112 ParFlow is an open source platform which realizes fully integrated surface-groundwater  
113 flow modeling (Kollet and Maxwell 2006; Maxwell et al. 2015). This parallel simulation  
114 platform has been widely used as a core hydrological module in hyperresolution land  
115 models (e.g., Maxwell and Kollet 2008; Maxwell and Condon 2016; Fang et al. 2017;  
116 Kurtz et al. 2016; Maxwell et al. 2011; Williams and Maxwell 2011; Shrestha et al. 2014).  
117 The brief description on the method of ParFlow to simulate integrated surface-subsurface  
118 water flows can be found below and the complete description of ParFlow can be found in  
119 Kollet and Maxwell (2006), Maxwell et al. (2015) and references therein.

120

121 In the subsurface, ParFlow solves the variably saturated Richards equation in three  
122 dimensions.

$$123 S_S S_W(h) \frac{\partial h}{\partial t} + \phi S_W(h) \frac{\partial S_W(h)}{\partial t} = \nabla \cdot \mathbf{q} + q_r \quad (1)$$

$$124 \mathbf{q} = -\mathbf{K}_s(\mathbf{x}) k_r(h) [\nabla(h+z) \cos \theta_x + \sin \theta_x] \quad (2)$$

125 In equation (1),  $h$  is the pressure head [L];  $z$  is the elevation with the  $z$  axis specified as  
126 upward [L];  $S_S$  is the specific storage [ $L^{-1}$ ];  $S_W$  is the relative saturation;  $\phi$  is the  
127 porosity [-];  $q_r$  is a general source/sink term. Equation (2) describes the flux term  $\mathbf{q}$   
128 [ $LT^{-1}$ ] based on Darcy's law, and  $\mathbf{K}_s$  is the saturated hydraulic conductivity tensor [ $LT^{-1}$ ]  
129  $^1$ ;  $k_r$  is the relative permeability [-];  $\theta$  is the local angle of topographic slope (see  
130 Maxwell et al. 2015). In this paper, the saturated hydraulic conductivity is assumed to be  
131 isotropic and the function of  $z$ :

$$132 \mathbf{K}_s = K_s(z) = K_{s,surface} \exp(-f(z_{surface} - z)) \quad (3)$$

133 where  $K_{s,surface}$  is the saturated hydraulic conductivity at the soil surface, and  $z_{surface}$   
134 is the elevation of the soil surface. The saturated hydraulic conductivity decreases  
135 exponentially as the soil depth increases (Beven 1982). The van Genuchten relationship  
136 (van Genuchten 1980) is used to describe the relative saturation and permeability  
137 functions.

138

139 Overland flow is solved by the two-dimensional kinematic wave equation. The dynamics  
140 of the surface ponding depth,  $h$  [L], can be described by:

$$141 \mathbf{k} \cdot [-K_s(z) k_r(h) \cdot \nabla(h+z)] = \frac{\partial \|h, 0\|}{\partial t} - \nabla \cdot \|h, 0\| \mathbf{v}_{sw} + q_r \quad (4)$$

142 In equation (4),  $\mathbf{k}$  is the unit vector in the vertical and  $\|a, b\|$  indicates the greater value  
 143 of the two quantities following the notation of Maxwell et al. (2015). If  $h < 0$ , equation  
 144 (4) describes that vertical fluxes across the land surface boundary is equal to a general  
 145 source/sink term  $q_r$  (i.e., rainfall and evapotranspiration). If  $h > 0$ , the terms on the right-  
 146 hand side of equation (4), which indicates water fluxes routed according to surface  
 147 topography, are active.  $\mathbf{v}_{sw}$  is the two-dimensional depth-averaged overland flow  
 148 velocity [ $LT^{-1}$ ] and estimated by the Manning's law:

$$149 \quad \mathbf{v}_{sw} = \begin{pmatrix} \frac{\sqrt{S_{f,x}}}{n} h^{\frac{2}{3}} \\ \frac{\sqrt{S_{f,y}}}{n} h^{\frac{2}{3}} \end{pmatrix} \quad (5)$$

150 where  $S_{f,x}$  and  $S_{f,y}$  are the friction slopes [-] for the x- and y-direction, respectively;  $n$   
 151 is the Manning's coefficient [ $TL^{-1/3}$ ]. In the kinematic wave approximation, the friction  
 152 slopes are set to the bed slopes. The methodology of discretization and numerical  
 153 implementation to solve equations (1-5) can be found in Kollet and Maxwell (2006).  
 154  
 155

## 156 2.2. Data Assimilation

157 In this paper, the ensemble Kalman filter (EnKF) was applied to assimilate soil moisture  
 158 observations into ParFlow. The general description of the Kalman filter is the following:

$$159 \quad \mathbf{x}^f(t) = \mathcal{M}[\mathbf{x}^a(t-1)] \quad (6)$$

$$160 \quad \mathbf{x}^a(t) = \mathbf{x}^f(t) + \mathbf{K}[y^o - \mathcal{H}\mathbf{x}^f(t)] \quad (7)$$

$$161 \quad \mathbf{K} = \mathbf{P}^f \mathcal{H}^T (\mathcal{H} \mathbf{P}^f \mathcal{H}^T + \mathbf{R})^{-1} \quad (8)$$

$$162 \quad \mathbf{P}^a = (\mathbf{I} - \mathbf{K} \mathcal{H}) \mathbf{P}^f \quad (9)$$

163 I follow the notation of Houtekamer and Zhang (2016). In equation (6), a forecast model  
 164  $\mathcal{M}$  (ParFlow in this study) is used to obtain a prior estimate at time  $t$ ,  $\mathbf{x}^f(t)$ , from the  
 165 estimation at the previous time  $\mathbf{x}^a(t-1)$ . In equation (7), a prior estimate  $\mathbf{x}^f(t)$  is  
 166 updated to the analysis state,  $\mathbf{x}^a(t)$ , using new observations  $y^o$ . The Kalman gain matrix  
 167  $\mathbf{K}$  calculated by equation (8) is used to give an appropriate weight between the  
 168 observations with an error covariance matrix  $\mathbf{R}$ , and the prior with an error covariance  
 169 matrix  $\mathbf{P}^f$ . To calculate  $\mathbf{K}$ , the observation operator  $\mathcal{H}$  is needed to map from model  
 170 space to observation space. It should be noted that the equations (6-9) give an optimal  
 171 estimation only when the error in model and observation follows the Gaussian distribution.  
 172 When the probabilistic distribution of the error in either model or observation has non-  
 173 Gaussian structure, results of the Kalman filter are suboptimal. This point is important to  
 174 interpret the results of this study.  
 175

176 EnKF is the Monte Carlo implementation of equations (6-9). To compute the Kalman gain  
 177 matrix,  $\mathbf{K}$ , ensemble approximations of  $\mathbf{P}^f \mathcal{H}^T$  and  $\mathcal{H} \mathbf{P}^f \mathcal{H}^T$  can be given by:

$$178 \quad \mathbf{P}^f \mathcal{H}^T \equiv \frac{1}{k-1} \sum_{i=1}^k (x_i^f - \bar{x}^f) (\mathcal{H} x_i^f - \overline{\mathcal{H} x^f})^T \quad (10)$$

$$179 \quad \mathcal{H} \mathbf{P}^f \mathcal{H}^T \equiv \frac{1}{k-1} \sum_{i=1}^k (\mathcal{H} x_i^f - \overline{\mathcal{H} x^f}) (\mathcal{H} x_i^f - \overline{\mathcal{H} x^f})^T \quad (11)$$

180 where  $x_i^f$  is the  $i$ th member of a  $k$ -member ensemble prior and  $\bar{x}^f = \frac{1}{k} \sum_{i=1}^k x_i^f$  and

$$181 \quad \overline{\mathcal{H} x^f} = \frac{1}{k} \sum_{i=1}^k \mathcal{H} x_i^f.$$

182

183 Once  $\bar{x}^a = \sum_{i=1}^k x_i^a$  ( $x_i^a$  is the  $i$ th member of a  $k$ -member ensemble analysis) and  $\mathbf{P}^a =$

184  $\frac{1}{k-1} \sum_{i=1}^k (x_i^a - \bar{x}^a) (x_i^a - \bar{x}^a)^T$  are computed by equations (6-11), there are still many

185 possible choices of an analysis ensemble. There are many proposed flavors of EnKF and

186 one of the main differences among them is how to choose the analysis ensemble  $x_i^a$ . In

187 this paper, the Ensemble Transform Kalman Filter (ETKF; Bishop et al. 2001; Hunt et al.

188 2007) was used to transport forecast ensembles to analysis ensembles.

189

190 In the ETKF, the analysis update for an ensemble mean is done by the following  
 191 equations:

$$192 \quad \tilde{\mathbf{P}}^a = [(k-1)I + (Y^f)^T R^{-1} Y^f]^{-1} \quad (12)$$

$$193 \quad \bar{w}^a = \tilde{\mathbf{P}}^a (Y^f)^T R^{-1} (y^o - \bar{y}^f) \quad (13)$$

$$194 \quad \bar{x}^a = \bar{x}^f + X^f \bar{w}^a \quad (14)$$

195 where the  $i$ th columns of  $Y^f$  and  $X^f$  are  $y_i^f - \bar{y}^f$  and  $x_i^f - \bar{x}^f$ , respectively.  $y_i^f$  is

196 defined by  $y_i^f = \mathcal{H} x_i^f$  and  $\bar{y}^f$  is the ensemble mean of  $y_i^f$ .  $I$  is the identity matrix.

197

198 The analysis covariance  $\mathbf{P}^a$  is given by:

$$199 \quad \mathbf{P}^a = \frac{1}{k-1} X^a (X^a)^T = X^f \tilde{\mathbf{P}}^a (X^f)^T \quad (15)$$

200 where the  $i$ th column of  $X^a$  is  $x_i^a - \bar{x}^a$ . The perturbations of the analysis ensemble

201 members can be generated by the square root of  $\tilde{\mathbf{P}}^a$ :

$$202 \quad W^a = [(k-1)\tilde{\mathbf{P}}^a]^{1/2} \quad (16)$$

$$203 \quad X^a = X^f W^a \quad (17)$$

204 Please refer to Hunt et al. (2007) for the complete description of the ETKF and its

205 localized version, the Local Ensemble Transform Kalman Filter (LETKF).

206

207 In many ensemble Kalman filter systems, the ensemble spread tends to become  
208 underdispersive without any ensemble inflation methods (Houtekamer and Zhang, 2016).  
209 In this paper, the relaxation to prior perturbation method (RTPP) of Zhang et al. (2004)  
210 was used to maintain an appropriate ensemble spread. In the RTPP, the computed analysis  
211 perturbations are relaxed back to the forecast perturbations:

$$212 x_{i,new}^a = (1 - \alpha)(x_i^a - \bar{x}^a) + \alpha(x_i^f - \bar{x}^f), \quad 0 \leq \alpha \leq 1 \quad (18)$$

213 where  $\alpha$  was set to 0.975 in this study.

214

215

### 216 **3. Experiment Design**

217 The synthetic experiment was implemented to examine how topography-driven surface  
218 lateral flows contribute to efficiently propagating observation's information horizontally  
219 in the data assimilation of soil moisture observation. Two synthetic reference runs were  
220 created by Parflow. The 2-D domain has a horizontal extension of 4000m and a vertical  
221 extension of 5m. The domain of the virtual slope was horizontally discretized into 40 grid  
222 cells with a grid cell size of 100m and vertically discretized into 50 grid cells with a grid  
223 cell size of 0.10m. The domain has a 25% slope. In two synthetic reference runs, it heavily  
224 rains only in the upper half of the slope ( $2000m < x < 4000m$ ). A constant rainfall rate of  
225 50mm/h was applied for 3 hours and then the period with no rainfall and evaporation of  
226 0.075mm/h lasted for 117 hours. This 120-hour rain/no rain cycle was repeatedly applied  
227 to the domain. The configurations described above were schematically shown in Figure  
228 1a. The parameters of the van Genuchten relationship, alpha and n, were set to 1.5 and  
229 1.75, respectively. The porosity,  $\phi$  in equation (1), was set to 0.40. The Manning's  
230 coefficient, n in equation (5), was set to  $5.52 \times 10^{-6} \text{ [m}^{-1/3}\text{h]}$ . The initial groundwater  
231 table was located in  $z=3m$  and the hydrostatic pressure gradient was assumed for the  
232 initial pressure heads in the unsaturated soil layers.

233

234 The difference between two synthetic reference runs is the value of saturated hydraulic  
235 conductivity. The surface saturated hydraulic conductivity,  $K_{s,surface}$  in equation (3),  
236 was set to 0.005 [m/h] in one reference, and 0.02 [m/h] in the other. Figure 1 shows the  
237 difference of the response to heavy rainfall between the two synthetic reference runs. In  
238 the case of the low saturated hydraulic conductivity (hereafter called the LOW\_K  
239 reference), larger surface lateral flows are generated than the case of the high saturated  
240 hydraulic conductivity (hereafter called the HIGH\_K reference). In the LOW\_K  
241 reference, the topography-driven surface lateral flows reach the left edge of the domain

242 (Figure 1b). In the HIGH\_K reference, supplied water moves vertically rather than  
243 horizontally and the topography-driven surface flows reach around  $x = 1000\sim 1500\text{m}$   
244 (Figure 1d).

245

246 For the data assimilation experiment, an ensemble of 50 realizations were generated. Each  
247 ensemble member has different saturated hydraulic conductivity and rainfall rate.  
248 Lognormal multiplicative noise was added to surface saturated hydraulic conductivity  
249 and rainfall rate of the synthetic reference runs. The two parameters of the lognormal  
250 distribution, commonly called  $\mu$  and  $\sigma$ , were set to 0 and 0.15, respectively. The initial  
251 groundwater depth of each ensemble member was drawn from the uniform distribution  
252 from 2.0m to 3.5m and the hydrostatic pressure gradient was assumed for the initial  
253 pressure heads in the unsaturated soil layers.

254

255 The virtual hourly observations were generated by adding the Gaussian white noise whose  
256 mean is zero to the volumetric soil moisture simulated by the synthetic reference runs.  
257 The observation error (the standard deviation of the added Gaussian white noise) was set  
258 to  $0.05 \text{ m}^3/\text{m}^3$ . It was assumed that the volumetric soil moistures can be observed in every  
259 soil layer from surface to the depth of 1m at the specific location. The two scenarios of  
260 the observation's location are provided. In the first scenario (hereafter called the UP\_O  
261 scenario), the volumetric soil moisture at the upper part of the slope ( $x = 2500\text{m}$ ) was  
262 observed. In the UP\_O scenario, I could observe the volumetric soil moisture in the upper  
263 part of the slope where it heavily rains and tried to infer the soil moisture in the lower part  
264 of the slope where it does not rain by propagating the observation's information downhill.  
265 In the second scenario (hereafter called the DOWN\_O scenario), the volumetric soil  
266 moisture at the lower part of the slope ( $x = 1500\text{m}$ ) was observed. In the DOWN\_O  
267 scenario, I could observe the volumetric soil moisture in the lower part of the slope where  
268 it does not rain and tried to infer the soil moisture in the upper part of the slope where it  
269 heavily rains by propagating the observation's information uphill.

270

271 Since I had the two synthetic reference runs (the HIGH\_K and LOW\_K references) and  
272 the two observation scenarios (the UP\_O and DOWN\_O scenarios), I implemented totally  
273 four data assimilation experiments. Table 1 summarizes the data assimilation experiments  
274 implemented in this study. For instance, in the HIGH\_K-UP\_O experiment, I chose the  
275 HIGH\_K reference and generated an ensemble of 50 realizations from the HIGH\_K  
276 reference. The soil moisture observations were generated from the HIGH\_K reference at  
277 the location of  $x = 2500\text{m}$  and assimilated into the model every hour. The simulated

278 volumetric soil moisture of the data assimilation experiment was compared with that of  
279 the HIGH\_K reference.

280

281 In the data assimilation experiments, I adjusted pressure head by data assimilation so that  
282  $x^f$  in section 2.2 is pressure head. Since the surface saturated hydraulic conductivity was  
283 also adjusted,  $x^f$  in section 2.2 includes  $K_{s,surface}$ . It should be noted that I adjusted a  
284 single surface saturated hydraulic conductivity which is applied to the whole domain so  
285 that the estimated parameter was not spatially distributed. Spatial regularization has been  
286 applied to calibrate spatially distributed parameters by adjusting a single parameter  
287 (Pokhrel and Gupta 2010). I suppose to apply the spatial regularization in the real-world  
288 application of the hyperresolution land data assimilation. Since I assimilated volumetric  
289 soil moisture observations ( $y^f$  and  $y^o$  in section 2.2 are simulated and observed  
290 volumetric soil moisture, respectively), the van Genuchten relationship works as an  
291 observation operator  $\mathcal{H}$  in this study.

292

293 In addition to the data assimilation (DA) experiments, I implemented the NoDA  
294 experiment (also called the open-loop experiment in the literatures of the LDAS study)  
295 in which the ensemble was used but no observation data were assimilated. As evaluation  
296 metrics, root-mean-square-error (RMSE) was used:

297 
$$RMSE = \sqrt{\frac{1}{k} \sum_{i=1}^k (F_i - T)^2} \quad (19)$$

298 where  $k$  is the ensemble number,  $F_i$  is the volumetric soil moisture simulated by the  $i$ -th  
299 member in the DA or NoDA experiment,  $T$  is the volumetric soil moisture simulated by  
300 the synthetic reference run.

301

302 To evaluate the impact of data assimilation, the improvement rate (IR) was defined and  
303 calculated by the following equation:

304 
$$IR = \frac{\overline{RMSE_{DA}} - \overline{RMSE_{NoDA}}}{\overline{RMSE_{NoDA}}} \quad (20)$$

305 where  $\overline{RMSE_{DA}}$  and  $\overline{RMSE_{NoDA}}$  are time-mean RMSE of the DA and NoDA  
306 experiments, respectively. The negative IR indicates that data assimilation positively  
307 impacts the simulation of soil moisture.

308

309 Four of 120-hour rain/no rain cycles were applied so that the computation period was 480  
310 hours. The spin-up results in the first 120 hours were not used to calculate the evaluation  
311 metrics.

#### 312 4. Results

313 Figure 2a shows the IR of the LOW\_K-UP\_O experiment. The time series of the DA and  
314 NoDA experiment and the synthetic reference run in the LOW\_K-UP\_O experiment can  
315 be found in Figure S1. The data assimilation efficiently propagates the information of the  
316 observations located in the upper part of the slope (see the black arrow in Figure 2a) both  
317 horizontally and vertically. RMSE is reduced by data assimilation not only directly under  
318 the observation but also the lower part of the slope where it does not rain. However, the  
319 increase of RMSE by data assimilation can be found at the left edge of the domain, which  
320 is far from the location of the observation. Please note that the impact of data assimilation  
321 on the surface soil moisture simulation is small because the RMSE of the NoDA  
322 experiment is already small ( $\leq 0.01\text{m}^3/\text{m}^3$ ) there in the case of the LOW\_K reference.

323

324 Figure 2b shows the IR of the LOW\_K-DOWN\_O experiment (see also Figure S2 for  
325 time series). The IR's spatial pattern of the LOW\_K-DOWN\_O experiment is similar to  
326 that of the LOW\_K-UP\_O experiment. It is promising that I can accurately infer soil  
327 moisture in the region where it heavily rains from the shallow soil moisture observations  
328 in the region where it does not rain.

329

330 Figure 3a shows the difference of time-mean RMSEs ( $\overline{RMSE_{DA}}$  in equation (20))  
331 between the LOW\_K-UP\_O and LOW\_K-DOWN\_O experiments. Although observing  
332 the lower part of the slope slightly improves the soil moisture simulation at the left edge  
333 of the domain compared with observing the upper part of the slope, there are few  
334 differences between the UP\_O and DOWN\_O scenarios in the case of the LOW\_K  
335 reference. In the data assimilation system of this study, the soil moisture observations  
336 have large representativeness and I can efficiently infer soil moisture in the soil columns  
337 which are horizontally and vertically far from the observations.

338

339 Figure 2c shows the IR of the HIGH\_K-UP\_O experiment (see also Figure S3 for time  
340 series). The data assimilation significantly reduces RMSE of the soil moisture simulation  
341 directly under the observations (see the black arrow in Figure 2c), which indicates that  
342 the data assimilation efficiently propagates the information of the observations vertically.  
343 However, the impact of the data assimilation on the soil moisture simulation in the lower  
344 part of the slope around  $x=1500\text{m}$  is marginal although there are large RMSE in the NoDA  
345 experiment ( $>0.05\text{m}^3/\text{m}^3$ ) at the edge of the area where topography-driven surface flows  
346 reach in the HIGH\_K reference (see Figure 1d).

347

348 Figure 2d shows the IR of the HIGH\_K-DOWN\_O experiment (see also Figure S4 for  
349 time series). Although the observations in the lower part of the slope (see the black arrow  
350 in Figure 2d) significantly improve the soil moisture simulation in the downstream area  
351 of the observation, the impact of the data assimilation on the shallow soil moisture  
352 simulation around  $x=500\sim 1000\text{m}$  is marginal. As I found in the LOW\_K-DOWN\_O  
353 experiment, the shallow soil moisture observations in the region where it does not rain  
354 can improve the soil moisture simulation in the region where it heavily rains. However,  
355 the IR of the HIGH\_K-DOWN\_O experiment in the upper part of the slope is smaller  
356 than that of the LOW\_K-DOWN\_O experiment (see Figure 2b and 2d).

357

358 The high representativeness of the observations which I found in the case of the LOW\_K  
359 reference cannot be found in the case of the HIGH\_K reference. Figure 3b shows the  
360 difference of time-mean RMSEs ( $\overline{RMSE}_{DA}$  in equation (20)) between the HIGH\_K-  
361 UP\_O and HIGH\_K-DOWN\_O experiments. Compared with the LOW\_K reference case  
362 (Figure 3a), there are significant differences between the UP\_O and DOWN\_O scenarios  
363 in the case of higher saturated hydraulic conductivity. In this case, the vertical propagation  
364 of the observations' information is more efficient than the horizontal propagation.

365

366 The relatively low efficiency of the data assimilation and the low representativeness of  
367 the soil moisture observations in the case of the HIGH\_K reference are caused by the  
368 non-Gaussian model error distribution. To evaluate the non-Gaussianity of the model  
369 error sampled by an ensemble, I used the Kullback-Leibler divergence (KLD) (Kullback  
370 and Leibler 1951):

$$371 \quad D_{KL}(p, q) = \sum_i p(i) \log \frac{p(i)}{q(i)} \quad (21)$$

372 where  $D_{KL}(p, q)$  is the KLD between two probabilistic distribution functions (PDFs),  $p$   
373 and  $q$ . If two PDFs are equal for all  $i$ ,  $D_{KL}(p, q) = 0$ . A large value for  $D_{KL}(p, q)$   
374 indicates that  $p$  and  $q$  are not close to each other. Therefore, the KLD is appropriate as  
375 a benchmark to evaluate the closeness of two PDFs. It should be noted that the KLD is  
376 not symmetric ( $D_{KL}(p, q) \neq D_{KL}(q, p)$ ). In this study, I compared the PDF of the NoDA  
377 ensemble ( $p$  in equation (21)) with the Gaussian PDF which has the mean and variance  
378 of the NoDA ensemble ( $q$  in equation (21)).

379

380 Figure 4 shows that the NoDA ensemble in the case of the HIGH\_K reference has stronger  
381 non-Gaussianity than the case of the LOW\_K reference especially in the shallow soil  
382 layers. The strong non-Gaussianity of the NoDA ensemble generated from the HIGH\_K

383 reference can be found at the edge of the area where topography-driven surface flows  
384 reach (Figure 1d). Figure 5 shows that there is the bifurcation of the ensemble in this  
385 region when the ensemble is generated from the HIGH\_K reference. The process of  
386 topography-driven surface flows is switched on if and only if the surface soil is saturated  
387 (see equation (4)) so that the ensemble tends to be bifurcated into the members with  
388 surface flows and without surface flows. As I mentioned in section 2.2, in the ETKF, the  
389 state and parameter variables are adjusted assuming the Gaussian PDF of the model's  
390 error and the linear relationship between observed variables and unobserved variables.  
391 Therefore, the non-Gaussianity of the prior ensemble induced by the strong non-linear  
392 dynamics of surface lateral flows makes the ETKF inefficient. It should be noted that the  
393 non-Gaussianity can also be found in the LOW\_K reference at the edge of the domain  
394 ( $x=500\text{m}$ ) due to the non-linear dynamics, which causes the degradation of the soil  
395 moisture simulation in the LOW\_K-UP\_O experiment (see Figure 2a).

396

397

## 398 **5. Discussion**

399 In this study, I revealed that the hyperresolution integrated surface-subsurface  
400 hydrological model gives the unique opportunity to effectively use soil moisture  
401 observations to improve the soil moisture simulation. I found that the explicit calculation  
402 of topography-driven surface flows has an important role in propagating the information  
403 of soil moisture observation horizontally by data assimilation even if there is considerable  
404 heterogeneity of meteorological forcing. It is possible that the soil moisture observations  
405 in the area where it does not heavily rain can improve the soil moisture simulation in the  
406 severe rainfall area. This potential cannot be brought out in the conventional 1-D LSM  
407 where sub-grid scale surface runoff is parameterized and the surface flows in one grid do  
408 not move to the adjacent grids. This new potential of hyperresolution land data  
409 assimilation is expected to be useful to monitor and predict flash floods induced by local  
410 severe rainfall on complex terrain.

411

412 However, I also found that the conventional ensemble data assimilation (i.e. ETKF)  
413 severely suffers from the non-Gaussian model error PDFs caused by the strongly  
414 nonlinear dynamics of topography-driven surface flows. The efficiency of ETKF to  
415 propagate the information of observations horizontally in the model space is limited when  
416 capacity of soil to hold water is high (i.e. high saturated hydraulic conductivity). It should  
417 be noted that the low representativeness of the soil moisture observations in the case of  
418 the HIGH\_K reference is due to the core assumption of the Kalman filter that the error

419 PDFs follow the Gaussian distribution so that the increase of the ensemble size cannot  
420 solve this issue. I implemented the data assimilation experiment in the case of the  
421 HIGH\_K reference with the 500 ensemble size, which is 10 times larger than the  
422 experiments shown in section 4, and found no significant improvement of the soil  
423 moisture simulation (not shown).

424

425 The results of the HIGH\_K-UP\_O and the HIGH\_K-DOWN\_O imply that the spatially  
426 dense soil moisture observations are needed to efficiently constrain state variables at the  
427 edge of surface flows. High resolution soil moisture remote sensing based on satellite  
428 active and passive combined microwave observations (e.g., He et al. 2018) and the  
429 assimilation of those data (Lievens et al. 2017) may be the important technologies in the  
430 era of the hyperresolution land modeling. The high resolution observations of surface  
431 inundated water from satellite imagery (e.g., Sakamoto et al. 2007 RSE; Arnesen et al.  
432 2013 RSE) may also be useful.

433

434 Since there is the nonlinear relationship between observed and unobserved variables  
435 sampled by an ensemble, a localization method, which spatially restricts the impact of  
436 assimilating observation, is crucially needed for the real-world application. The results of  
437 this study imply that the optimal localization radius strongly depends on the model  
438 parameter (i.e. saturated hydraulic conductivity). Rasmussen et al. (2015) successfully  
439 applied the adaptive localization method (Anderson 2007; Bishop and Hodyss 2009) to  
440 the data assimilation of groundwater observations into a hydrological model. It is  
441 appropriate to adaptively determine the localization radius considering the lack of prior  
442 knowledge of how soil moistures simulated by an ensemble are horizontally correlated.

443

444 Reducing the uncertainty in rainfall positively impacts the efficiency of data assimilation  
445 since the bifurcation of simulated soil moisture found in Figure 5c is originally induced  
446 by the uncertainty in rainfall. Although assimilating land hydrological observations to  
447 improve the rainfall input has been intensively investigated (e.g., Sawada et al. 2018;  
448 Herrnegger et al. 2015; Crow et al. 2011; Vrugt et al. 2008), it has yet to be applied to the  
449 hyperresolution land models. It should be noted that the parameters of the lognormal  
450 distribution to model the uncertainty in rainfall were specified to make the rainfall PDF  
451 similar to the Gaussian distribution. I chose the lognormal distribution in order not to  
452 generate the negative value of rainfall and I did not intend to introduce non-Gaussianity  
453 into the external forcing. The rainfall input which follows the Gaussian PDF was

454 transformed into the non-Gaussian PDF of the model error by the strongly nonlinear  
455 dynamics of topography-driven surface flows.

456

457 To explicitly consider the non-Gaussianity and non-linear relationship between observed  
458 and unobserved variables induced by topography-driven surface flows, the particle filters  
459 may be useful. The particle filtering can represent a probability distribution (including  
460 non-Gaussian distributions) directly by an ensemble. The particle filters have been  
461 intensively applied to conventional 1-D LSMs (e.g., Sawada et al. 2015; Qin et al. 2009)  
462 and lumped hydrological models (e.g., Yan and Moradkhani 2016; Vrugt et al. 2013).  
463 Although particle filtering in the high dimensional system suffers from the “curse of  
464 dimensionality” (e.g., Snyder et al. 2008), the applicability of particle filtering to the 3-D  
465 hyperresolution land models should be assessed in the future.

466

467 Since the synthetic numerical experiment implemented in this paper assumed the extreme  
468 heterogeneity of rainfall, the findings of this paper may be exaggerated. In the future work,  
469 the contributions of the topography-driven surface runoff process to the data assimilation  
470 of hydrological observations should be quantified in the real-world application. In  
471 addition, in the virtual experiment of this paper, I neglected some of the important land  
472 processes such as transpiration, canopy interception, snow, and frozen soil. Although they  
473 are generally not important processes in terms of the generation of topography-driven  
474 surface lateral flows, those processes should be considered in the future.

475

476

## 477 **6. Conclusions**

478 Lateral surface flows induced by heavy rainfalls do matter for data assimilation of soil  
479 moisture observations into hyperresolution land models. Even if there is extreme  
480 heterogeneity of rainfall, I can effectively propagate the information of the soil moisture  
481 observations horizontally in the model space and improve the soil moisture simulation by  
482 the ensemble Kalman filter. This new capability of the data assimilation with the  
483 hyperresolution land models may innovate the monitor and prediction of flash floods  
484 caused by local severe rainfalls. However, the non-Gaussianity of the model error induced  
485 by the nonlinear dynamics of topography-driven surface flows harms the efficiency of the  
486 data assimilation of soil moisture observations. When topography-driven surface slope  
487 runoff exists, the efficiency of assimilating shallow soil moisture observations into the  
488 hyperresolution land models depends on soil characteristics of the study area.

489

490

## 491 **Acknowledgement**

492 All data used in this paper are stored in the repository of Meteorological Research  
493 Institute for 5 years and available upon request to Y. Sawada. The ETKF code used in this  
494 study is based on the open source available at <https://github.com/takemasa-miyoshi/letkf>.  
495 This study was supported by the JSPS KAKENHI grant JP17K18352.

496

## 497 **References**

498

499 Ait-El-Fquih, B., El Gharamti, M., & Hoteit, I. (2016). A Bayesian consistent dual  
500 ensemble Kalman filter for state-parameter estimation in subsurface hydrology.  
501 *Hydrology and Earth System Sciences*, 20(8), 3289–3307. [https://doi.org/10.5194/hess-](https://doi.org/10.5194/hess-20-3289-2016)  
502 20-3289-2016

503

504 Amesen et al. (2013). Monitoring flood extent in the lower Amazon River floodplain  
505 using ALOS/PALSAR ScanSAR images. *Remote Sensing of Environment*, 130, 51-61.  
506 <https://doi.org/10.1016/j.rse.2012.10.035>

507

508 Anderson, J. L. (2007). Exploring the need for localization in ensemble data assimilation  
509 using a hierarchical ensemble filter. *Physica D: Nonlinear Phenomena*, 230(1–2), 99–111.  
510 <https://doi.org/10.1016/j.physd.2006.02.011>

511

512 Bandara, R., Walker, J. P., & Rüdiger, C. (2014). Towards soil property retrieval from  
513 space: Proof of concept using in situ observations. *Journal of Hydrology*, 512, 27–38.  
514 <https://doi.org/10.1016/j.jhydrol.2014.02.031>

515

516 Bandara, R., Walker, J. P., Rüdiger, C., & O. Merlin (2015). Towards soil property  
517 retrieval from space: An application with disaggregated satellite observations. *Journal of*  
518 *Hydrology*, 522, 582-593, <https://doi.org/10.1016/j.jhydrol.2015.01.018>

519

520 Beven, K. (1982), On subsurface stormflow: an analysis of response times, *Hydrological*  
521 *Science Journal*, 27, 505-521, doi:10.1080/02626668209491129

522

523 Bishop, C.H., Etherton, B., J., & Majumdar, S., J., (2001). Adaptive Sampling with the  
524 Ensemble Transform Kalman Filter. Part I: Theoretical Aspects. *Monthly. Weather.*

525 *Review*, **129**, 420–436, [https://doi.org/10.1175/1520-](https://doi.org/10.1175/1520-0493(2001)129<0420:ASWTET>2.0.CO;2)  
526 [0493\(2001\)129<0420:ASWTET>2.0.CO;2](https://doi.org/10.1175/1520-0493(2001)129<0420:ASWTET>2.0.CO;2)

527

528 Bishop, C. H., & Hodyss, D., (2009) Ensemble covariances adaptively localized with  
529 ECO-RAP. Part 1: Tests on simple error models. *Tellus*, *61A*, 84–96.

530

531 Camporese, M., Paniconi, C., Putti, M., & Salandin, P. (2009). Ensemble Kalman filter  
532 data assimilation for a process-based catchment scale model of surface and subsurface  
533 flow. *Water Resources Research*, *45*(10), 1–14. <https://doi.org/10.1029/2008WR007031>

534

535 Camporese, M., Paniconi, C., Putti, M., & Orlandini, S. (2010). Surface-subsurface flow  
536 modeling with path-based runoff routing, boundary condition-based coupling, and  
537 assimilation of multisource observation data. *Water Resources Research*, *46*(2).  
538 <https://doi.org/10.1029/2008WR007536>

539

540 Crow, W. T., Van Den Berg, M. J., Huffman, G. J., & Pellarin, T. (2011). Correcting  
541 rainfall using satellite-based surface soil moisture retrievals: The Soil Moisture Analysis  
542 Rainfall Tool (SMART). *Water Resources Research*, *47*(8), 1–15.  
543 <https://doi.org/10.1029/2011WR010576>

544

545 Fang, Y., L. R. Leung, Z. Duan, M. S. Wigmosta, R. M. Maxwell, J. Q. Chambers, & J.  
546 Tomasella (2017), Influence of landscape heterogeneity on water available to tropical  
547 forests in an Amazonian catchment and implications for modeling drought response, *J.*  
548 *Geophys. Res. Atmos.*, *122*, doi:10.1002/2017JD027066.

549

550 Han, X., Franssen, H.-J. H., Montzka, C. & Vereecken, H. (2014). Soil moisture and soil  
551 properties estimation in the Community Land Model with synthetic brightness  
552 temperature observations, *Water Resources Research.*, *50*, 6081 - 6105,  
553 doi:10.1002/2013WR014586.

554

555 Herrnegger, M., Nachtnebel, H. P., & Schulz, K. (2015). From runoff to rainfall : inverse  
556 rainfall – runoff modelling in a high temporal resolution, 4619–4639.  
557 <https://doi.org/10.5194/hess-19-4619-2015>

558

559 He, L., Hong, Y., Wu, X., Ye, N., Walker, J. P. & Chen, X. (2018). Investigation of SMAP  
560 Active–Passive Downscaling Algorithms Using Combined Sentinel-1 SAR and SMAP

561 Radiometer Data. *IEEE Transactions on Geosciences and Remote Sensing*, 56, 4906-  
562 4918, doi: [10.1109/TGRS.2018.2842153](https://doi.org/10.1109/TGRS.2018.2842153).  
563

564 Hendricks Franssen, H. J., & Kinzelbach, W. (2008). Real-time groundwater flow  
565 modeling with the Ensemble Kalman Filter: Joint estimation of states and parameters and  
566 the filter inbreeding problem. *Water Resources Research*, 44(9), 1–21.  
567 <https://doi.org/10.1029/2007WR006505>  
568

569 Houborg, R., Rodell, M., Li, B., Reichle, R., & Zaitchik, B. F. (2012). Drought indicators  
570 based on model-assimilated Gravity Recovery and Climate Experiment (GRACE)  
571 terrestrial water storage observations. *Water Resources Research*, 48(7).  
572 <https://doi.org/10.1029/2011WR011291>  
573

574 Houtekamer, P. L., & Zhang, F. (2016). Review of the Ensemble Kalman Filter for  
575 Atmospheric Data Assimilation. *Monthly Weather Review*, MWR-D-15-0440.1.  
576 <https://doi.org/10.1175/MWR-D-15-0440.1>  
577

578 Hunt, B. R., Kostelich, E. J., & Szunyogh, I. (2007). Efficient data assimilation for  
579 spatiotemporal chaos: A local ensemble transform Kalman filter. *Physica D: Nonlinear*  
580 *Phenomena*, 230(1–2), 112–126. <https://doi.org/10.1016/j.physd.2006.11.008>  
581

582 Ji, P., Yuan, X., & Liang, X. Z. (2017). Do Lateral Flows Matter for the Hyperresolution  
583 Land Surface Modeling? *Journal of Geophysical Research: Atmospheres*, 1–16.  
584 <https://doi.org/10.1002/2017JD027366>  
585

586 Keune, J., F. Gasper, K. Goergen, A. Hense, P. Shrestha, M. Sulis, & S. Kollet (2016),  
587 Studying the influence of groundwater representations on land surface-atmosphere  
588 feedbacks during the European heat wave in 2003, *Journal of Geophysical Research.*  
589 *Atmospheres*, 121, 13,301–13,325, doi:10.1002/2016JD025426.  
590

591 Kollet, S. J., & Maxwell, R. M. (2006). Integrated surface–groundwater flow modeling:  
592 A free-surface overland flow boundary condition in a parallel groundwater flow model.  
593 *Advances in Water Resources*, 29(7), 945–958.  
594 <https://doi.org/10.1016/j.advwatres.2005.08.006>  
595

596 Kumar, S. V., Reichle, R. H., Koster, R. D., Crow, W. T., & Peters-Lidard, C. D. (2009).  
597 Role of Subsurface Physics in the Assimilation of Surface Soil Moisture Observations.  
598 *Journal of Hydrometeorology*, 10(6), 1534–1547.  
599 <https://doi.org/10.1175/2009JHM1134.1>  
600

601 Kurtz, W., He, G., Kollet, S. J., Maxwell, R. M., Vereecken, H., & Franssen, H. J. H.  
602 (2016). TerrSysMP-PDAF (version 1.0): A modular high-performance data assimilation  
603 framework for an integrated land surface-subsurface model. *Geoscientific Model*  
604 *Development*, 9(4), 1341–1360. <https://doi.org/10.5194/gmd-9-1341-2016>  
605

606 Kullback, S., & Leibler, R. A. (1951). On information and sufficiency, *The Annals of*  
607 *Mathematical Statistics*, 22, 79-86  
608

609 Lawrence, D. M., et al. (2011). Parameterization improvements and functional and  
610 structural advances in Version 4 of the Community Land Model. *Journal of Advances in*  
611 *Modeling Earth Systems*, 3(3), 1–27. <https://doi.org/10.1029/2011MS000045>  
612

613 Li, B., Rodell, M., Zaitchik, B. F., Reichle, R. H., Koster, R. D., & van Dam, T. M. (2012).  
614 Assimilation of GRACE terrestrial water storage into a land surface model: Evaluation  
615 and potential value for drought monitoring in western and central Europe. *Journal of*  
616 *Hydrology*, 446–447, 103–115. <https://doi.org/10.1016/j.jhydrol.2012.04.035>  
617

618 Lievens, et al. (2017). Joint Sentinel-1 and SMAP data assimilation to improve soil  
619 moisture estimates. *Geophysical Research Letters*, 44(12), 6145–6153.  
620 <https://doi.org/10.1002/2017GL073904>  
621

622 Martens, B., Miralles, D. G., Lievens, H., Schalie, R. Van Der, & Jeu, R. A. M. De. (2017).  
623 GLEAM v3 : satellite-based land evaporation and root-zone soil moisture, *Geoscientific*  
624 *Model Development*, 10, 1903–1925. <https://doi.org/10.5194/gmd-10-1903-2017>  
625

626 Maxwell, R. M., & N. L. Miller (2005). Development of a Coupled Land Surface and  
627 Groundwater Model. *Journal of Hydrometeorology*, 6, 233-247.  
628 <https://doi.org/10.1175/JHM422.1>  
629

630 Maxwell, R. M., & Condon, L. E. (2016). Connections between groundwater flow and  
631 transpiration partitioning. *Science*, 353, 377-380, doi: 10.1126/science.aaf7891.

632

633 Maxwell, R. M., Condon, L. E., & Kollet, S. J. (2015). A high-resolution simulation of  
634 groundwater and surface water over most of the continental US with the integrated  
635 hydrologic model ParFlow v3, 923–937. <https://doi.org/10.5194/gmd-8-923-2015>

636

637 Maxwell, R. M., & Kollet, S. J. (2008). Interdependence of groundwater dynamics and  
638 land-energy feedbacks under climate change, *Nature Geoscience*, *1*, 665–669.  
639 <https://doi.org/10.1038/ngeo315>

640

641 Maxwell, R. M., Lundquist, J. K., Mirocha, J. D., Smith, S. G., Woodward, C. S., &  
642 Tompson, A. F. B. (2011). Development of a Coupled Groundwater–Atmosphere Model.  
643 *Monthly Weather Review*, *139*(1), 96–116. <https://doi.org/10.1175/2010MWR3392.1>

644

645 Nerger, L., & Hiller, W., (2013). Software for ensemble-based data assimilation systems  
646 – implementation strategies and scalability. *Computers & Geosciences*. *55*, 110–118.  
647 <http://dx.doi.org/10.1016/j.cageo.2012.03.026>

648

649 Niu, G. Y., Paniconi, C., Troch, P. a., Scott, R. L., Durcik, M., Zeng, X., & Goodrich, D.  
650 C. (2014). An integrated modelling framework of catchment-scale ecohydrological  
651 processes: 1. Model description and tests over an energy-limited watershed.  
652 *Ecohydrology*, *7*(2), 427–439. <https://doi.org/10.1002/eco.1362>

653

654 Pokhrel, P., & Gupta, H. V. (2010). On the use of spatial regularization strategies to  
655 improve calibration of distributed watershed models. *Water Resources Research*, *46*(1),  
656 1–17. <https://doi.org/10.1029/2009WR008066>

657

658 Qin, J., Liang, S., Yang, K., Kaihotsu, I., Liu, R., & Koike, T. (2009). Simultaneous  
659 estimation of both soil moisture and model parameters using particle filtering method  
660 through the assimilation of microwave signal. *Journal of Geophysical Research*,  
661 *114*(D15), 1–13. <https://doi.org/10.1029/2008JD011358>

662

663 Rasmussen, J., Madsen, H., Jensen, K. H., & Refsgaard, J. C. (2015). Data assimilation  
664 in integrated hydrological modeling using ensemble Kalman filtering: evaluating the  
665 effect of ensemble size and localization on filter performance. *Hydrology and Earth  
666 System Sciences*, *19*(7), 2999–3013. <https://doi.org/10.5194/hess-19-2999-2015>

667

668 Sakamoto, T., et al. (2007). Detecting temporal changes in the extent of annual flooding  
669 within the Cambodia and the Vietnamese Mekong Delta from MODIS time-series  
670 imagery. *Remote Sensing of Environment*, 109, 295-313.  
671 <https://doi.org/10.1016/j.rse.2007.01.011>.  
672

673 Sawada, Y. & Koike, T. (2014). Simultaneous estimation of both hydrological and  
674 ecological parameters in an eco-hydrological model by assimilating microwave signal,  
675 *Journal of Geophysical Research – Atmospheres*, 119, 8839-8857,  
676 <https://doi.org/10.1002/2014JD021536>  
677

678 Sawada, Y., Koike, T., & Walker, J. P. (2015). A land data assimilation system for  
679 simultaneous simulation of soil moisture and vegetation dynamics, *Journal of*  
680 *Geophysical Research – Atmospheres*, 120, 5910-5930,  
681 <https://doi.org/10.1002/2014JD022895>  
682

683 Sawada, Y., Nakaegawa, T., & Miyoshi, T. (2018) Hydrometeorology as an inversion  
684 problem: Can river discharge observations improve the atmosphere by ensemble data  
685 assimilation?, *Journal of Geophysical Research - Atmospheres*, 123, 848-860,  
686 <https://doi.org/10.1002/2017JD027531>  
687

688 Sellers, P. J., et al. (1996). A revised land surface parameterization (SiB2) for atmospheric  
689 GCMs. Part I: Model formulation. *Journal of Climate*. [https://doi.org/10.1175/1520-  
690 0442\(1996\)009<0676:ARLSPF>2.0.CO;2](https://doi.org/10.1175/1520-0442(1996)009<0676:ARLSPF>2.0.CO;2)  
691

692 Shrestha, P., Sulis, M., Masbou, M., Kollet, S., & Simmer, C. (2014). A Scale-Consistent  
693 Terrestrial Systems Modeling Platform Based on COSMO, CLM, and ParFlow. *Monthly*  
694 *Weather Review*, 142(9), 3466–3483. <https://doi.org/10.1175/MWR-D-14-00029.1>  
695

696 Snyder, C., Bengtsson, T., Bickel, P., & Anderson, J. (2008). Obstacles to High-  
697 Dimensional Particle Filtering. *Monthly Weather Review*, 136(12), 4629–4640.  
698 <https://doi.org/10.1175/2008MWR2529.1>  
699

700 Tian, W., Li, X., Cheng, G. D., Wang, X. S., & Hu, B. X. (2012). Coupling a groundwater  
701 model with a land surface model to improve water and energy cycle simulation.  
702 *Hydrology and Earth System Sciences*, 16(12), 4707–4723. [https://doi.org/10.5194/hess-  
703 16-4707-2012](https://doi.org/10.5194/hess-16-4707-2012)

704

705 Van Genuchten, M. T. (1980), A closed-form equation for predicting the hydraulic  
706 conductivity of unsaturated soils, *Soil Science Society of America Journal*, 44, 892–898.

707

708 Verbeeck, H., Peylin, P., Bacour, C., Bonal, D., Steppe, K., & Ciais, P. (2011). fluxes in  
709 Amazon forests: Fusion of eddy covariance data and the ORCHIDEE model. *Journal of*  
710 *Geophysical Research*, 116(G2), 1–19. <https://doi.org/10.1029/2010JG001544>

711

712 Vrugt, J. A., ter Braak, C. J. F., Clark, M. P., Hyman, J. M., & Robinson, B. A. (2008).  
713 Treatment of input uncertainty in hydrologic modeling: Doing hydrology backward with  
714 Markov chain Monte Carlo simulation. *Water Resources Research*, 44, 1–15.  
715 <https://doi.org/10.1029/2007WR006720>

716

717 Vrugt, J. A., ter Braak, C. J. F., Diks, C. G. H., & Schoups, G. (2013). Hydrologic data  
718 assimilation using particle Markov chain Monte Carlo simulation: Theory, concepts and  
719 applications. *Advances in Water Resources*, 51, 457–478.  
720 <https://doi.org/10.1016/j.advwatres.2012.04.002>

721

722 Williams, J. L., & Maxwell, R. M. (2011). Propagating Subsurface Uncertainty to the  
723 Atmosphere Using Fully Coupled Stochastic Simulations. *Journal of Hydrometeorology*,  
724 12(4), 690–701. <https://doi.org/10.1175/2011JHM1363.1>

725

726 Yan, H., & Moradkhani, H. (2016). Combined assimilation of streamflow and satellite  
727 soil moisture with the particle filter and geostatistical modeling. *Advances in Water*  
728 *Resources*, 94, 364–378. <https://doi.org/10.1016/j.advwatres.2016.06.002>

729

730 Yang, K., Koike, T., Kaihotsu, I., & Qin, J. (2009). Validation of a Dual-Pass Microwave  
731 Land Data Assimilation System for Estimating Surface Soil Moisture in Semiarid  
732 Regions. *Journal of Hydrometeorology*, 10(3), 780–793.  
733 <https://doi.org/10.1175/2008JHM1065.1>

734

735 Yang, K., Watanabe, T., Koike, T., Li, X., Fujii, H., Tamagawa, K., & Ishikawa, H. (2007).  
736 Auto-calibration System Developed to Assimilate AMSR-E Data into a Land Surface  
737 Model for Estimating Soil Moisture and the Surface Energy Budget. *Journal of the*  
738 *Meteorological Society of Japan*, 85A, 229–242. <https://doi.org/10.2151/jmsj.85A.229>

739

740 Zhang, F., Snyder, C., & Sun, J. (2004). Impacts of Initial Estimate and Observation  
741 Availability on Convective-Scale Data Assimilation with an Ensemble Kalman Filter.  
742 *Monthly. Weather. Review.*, **132**, 1238–1253, [https://doi.org/10.1175/1520-](https://doi.org/10.1175/1520-0493(2004)132<1238:IOIEAO>2.0.CO;2)  
743 [0493\(2004\)132<1238:IOIEAO>2.0.CO;2](https://doi.org/10.1175/1520-0493(2004)132<1238:IOIEAO>2.0.CO;2)

744

745 Zhang, H., Kurtz, W., Kollet, S., Vereecken, H., & Franssen, H. J. H. (2018). Comparison  
746 of different assimilation methodologies of groundwater levels to improve predictions of  
747 root zone soil moisture with an integrated terrestrial system model. *Advances in Water*  
748 *Resources*, *III*(May 2017), 224–238. <https://doi.org/10.1016/j.advwatres.2017.11.003>

749

750

751

752

753

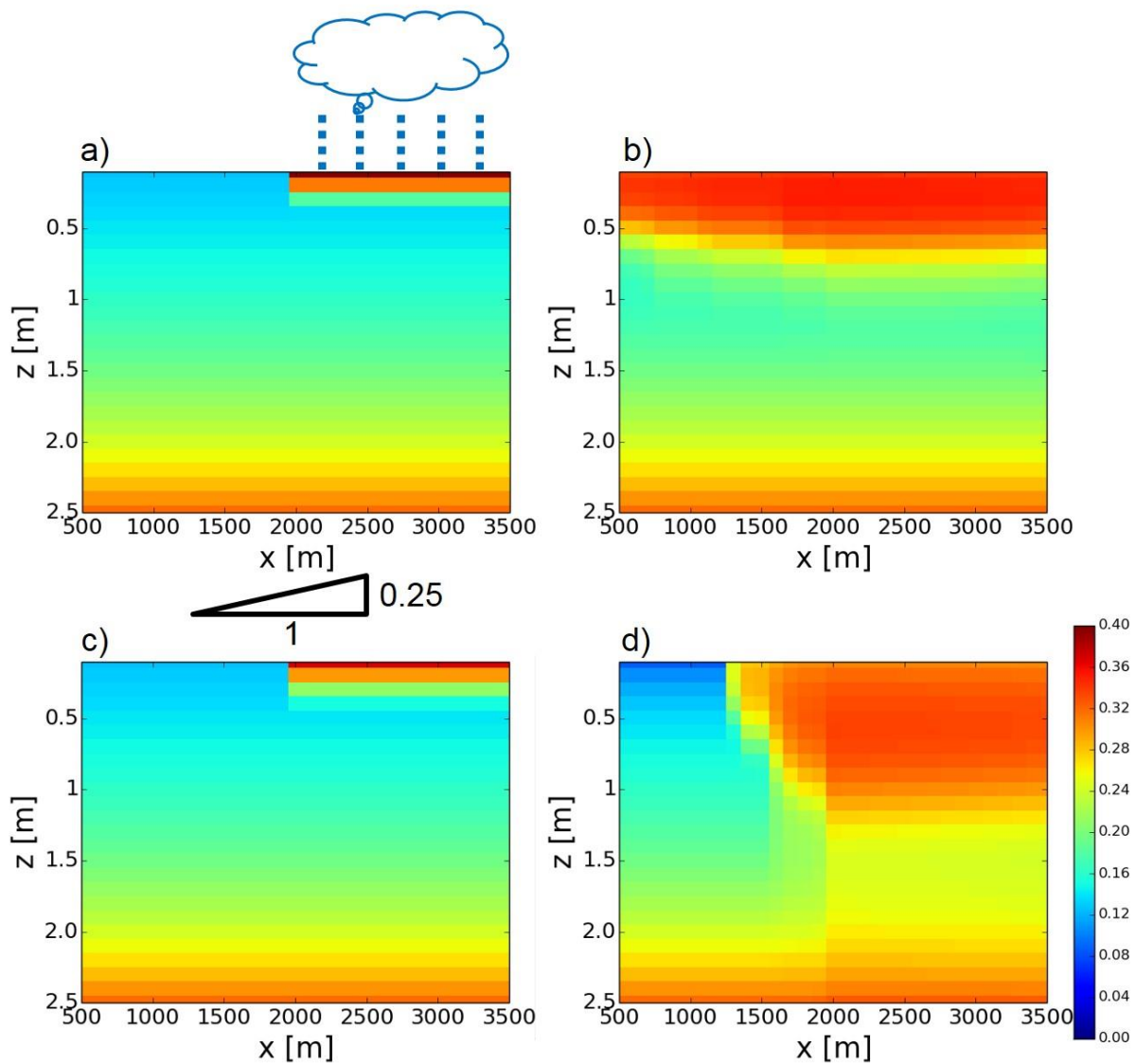
754

**Table 1.** Configuration of the data assimilation experiments

	hydraulic conductivity [m/h]	observation's location [m]
LOW_K-UP_O	0.005	2500
LOW_K-DOWN_O	0.005	1500
HIGH_K-UP_O	0.02	2500
HIGH_K-DOWN_O	0.02	1500

755

756



758

759

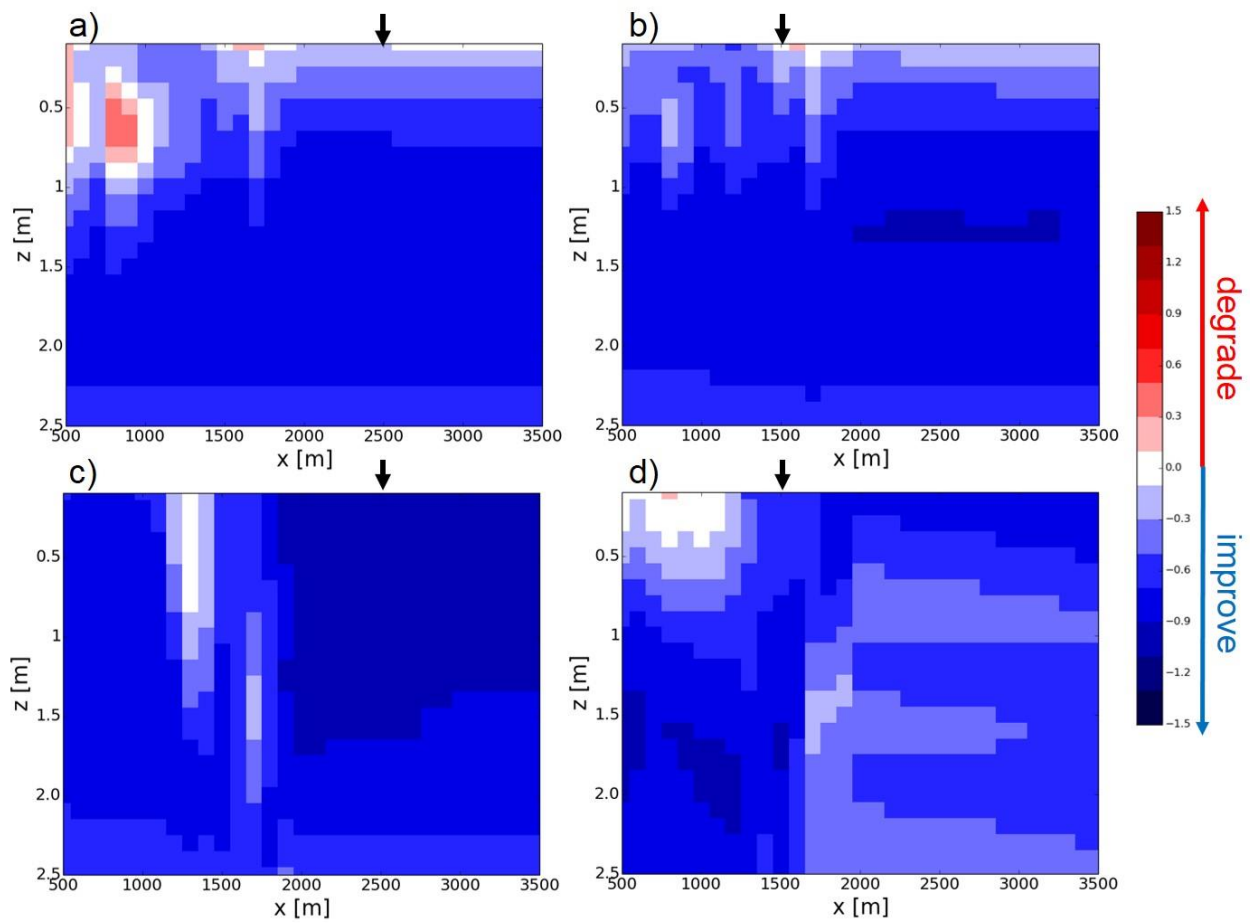
760

761

762

763

**Figure 1.** Distributions of volumetric soil moisture simulated by the synthetic reference runs. (a) The distribution of volumetric soil moisture [ $\text{m}^3/\text{m}^3$ ] simulated by the LOW\_K synthetic reference run at  $t = 0$ h. The schematic of the configuration of the synthetic reference runs is also shown (see also section 3). (b) same as (a) but at  $t = 130$ h. (c,d) same as (a,c) but for the HIGH\_K synthetic reference run.



764

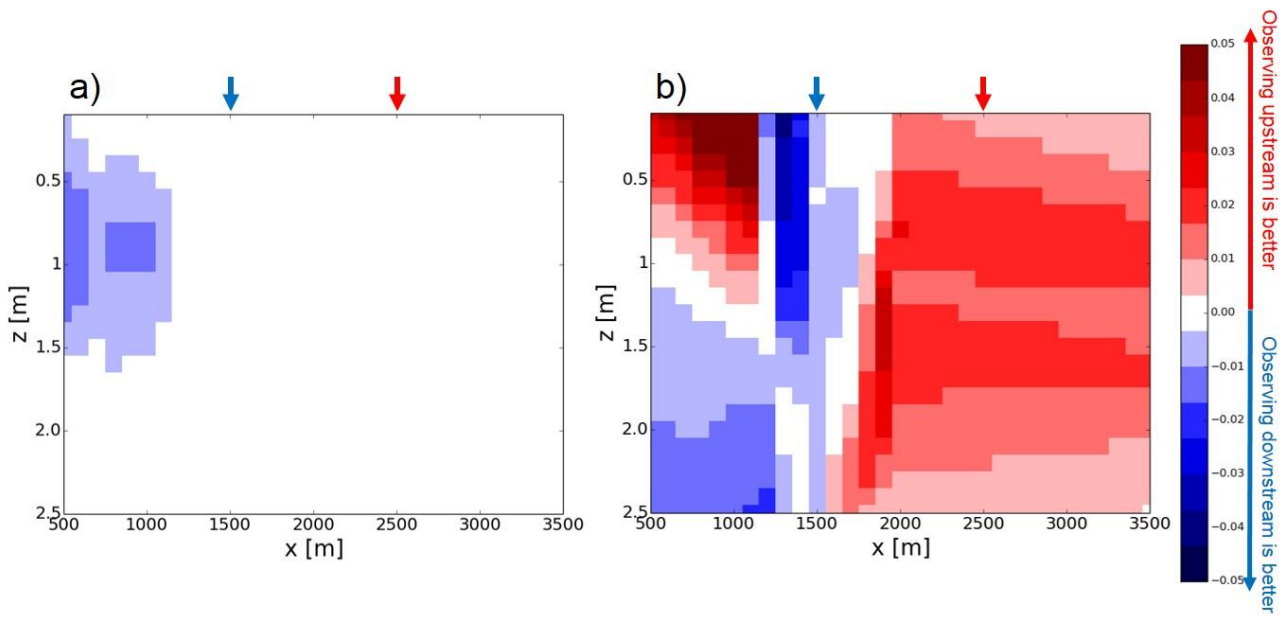
765

766

767

768

**Figure 2.** The improvement rates of the (a) LOW\_K-UP\_O, (b) LOW\_K-DOWN\_O, (c) HIGH\_K\_UP\_O, (d) HIGH\_K-DOWN\_O experiments (see Table 1 and section 3). Black arrows show the locations of the soil moisture observations in each experiment.



769

770

771

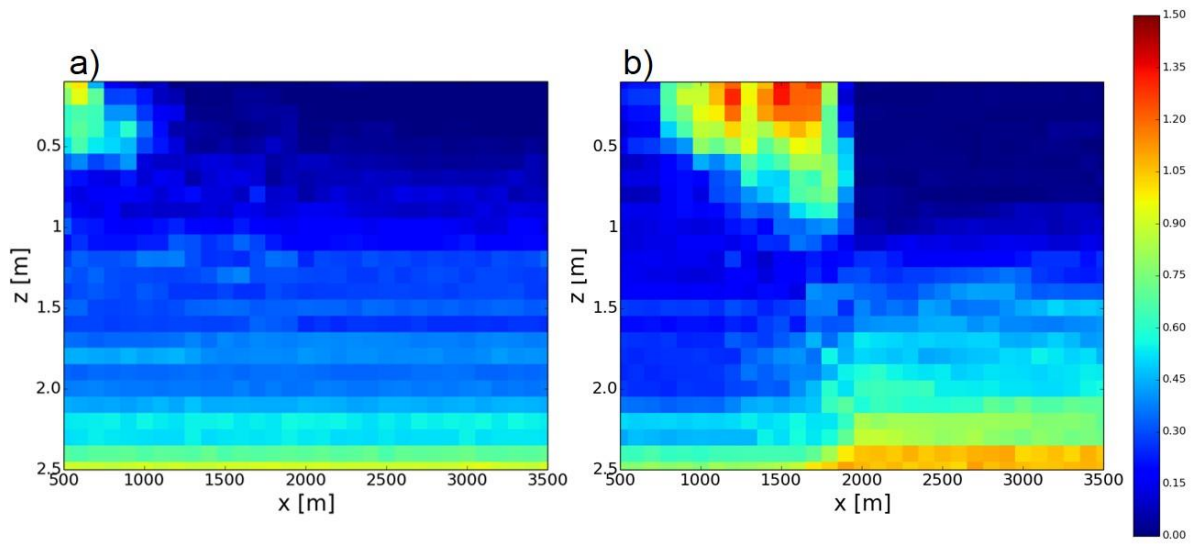
772

773

774

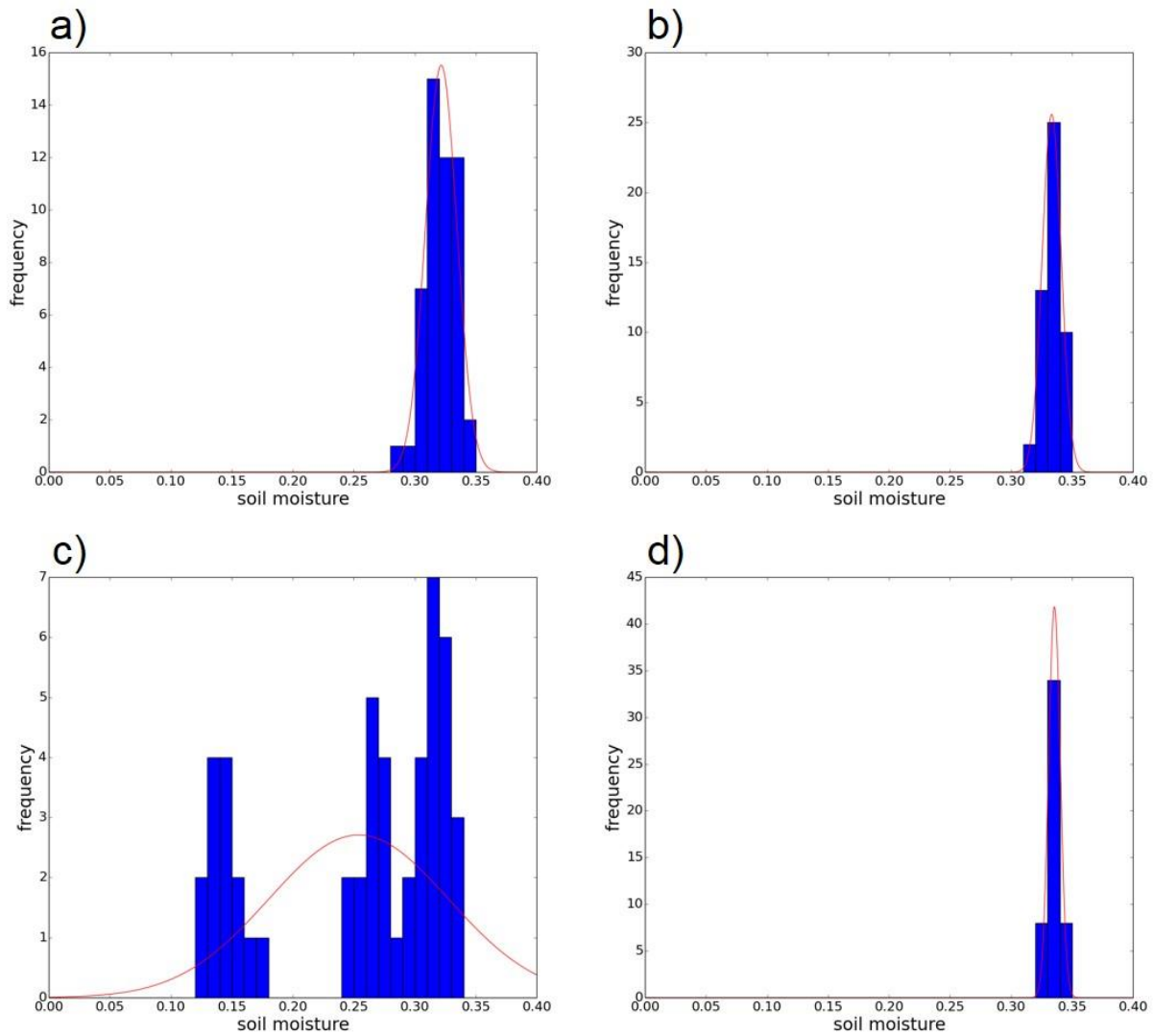
775

**Figure 3.** (a) The difference of time-mean RMSEs between the LOW\_K-UP\_O and LOW\_K-DOWN\_O experiments (see Table 1 and section 3). Red (blue) color indicates that the observations in the upper (lower) part of the slope reduce time-mean RMSE by data assimilation better than those in the lower (upper) part of the slope (see also arrows which are the locations of the observations). (b) same as (a) but for the difference between the HIGH\_K-UP\_O and HIGH\_K-DOWN\_O experiments.



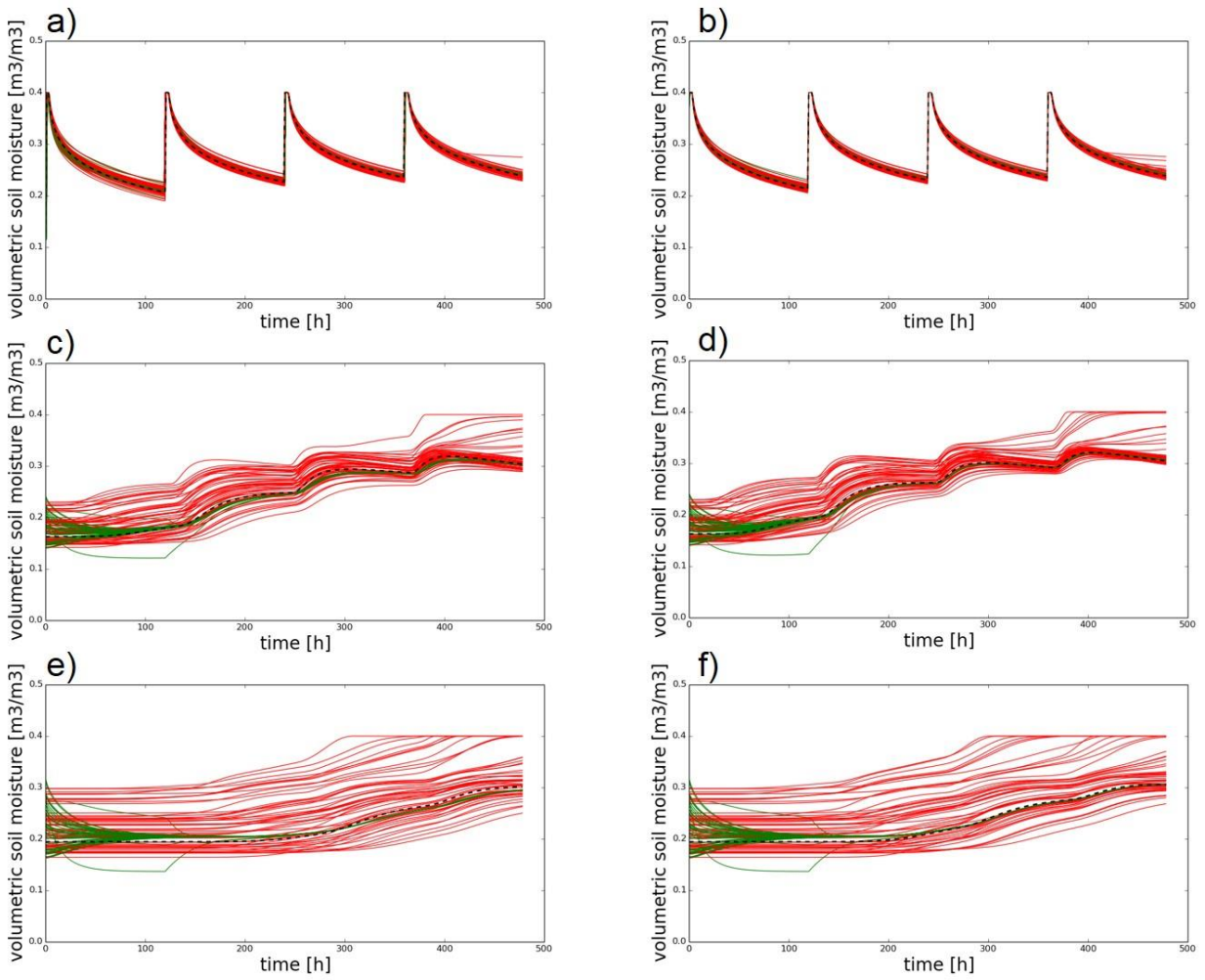
776  
777  
778  
779

**Figure 4.** The Kullback-Leibler divergence of the NoDA experiment generated by (a) the LOW\_K reference and (b) the HIGH\_K reference at  $t = 130\text{h}$  (see also Figure 1b and 1d).



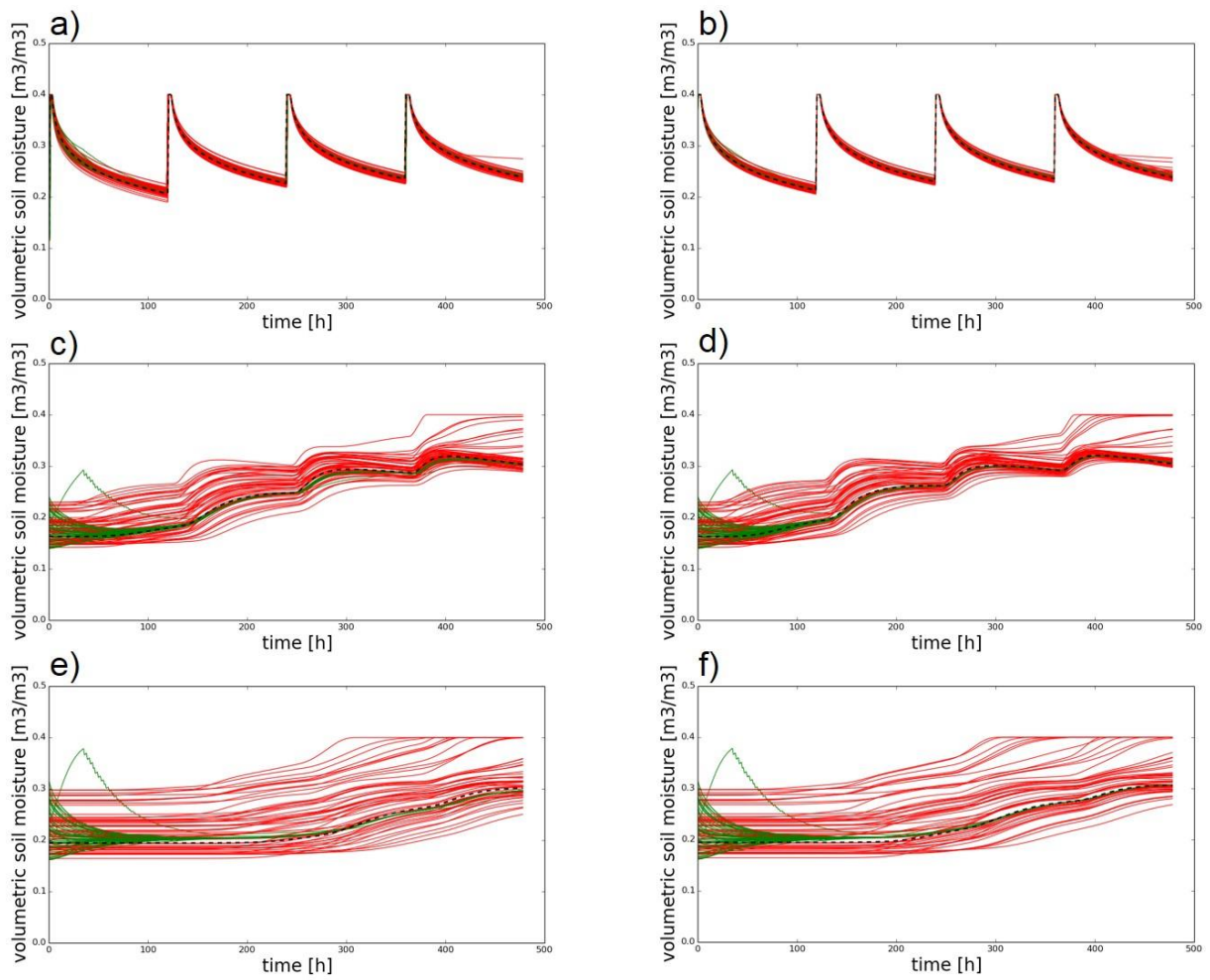
780  
781  
782  
783  
784  
785  
786

**Figure 5.** (a) The histogram (blue bars) of the volumetric soil moisture simulated by the NoDA experiment (see section 3) with the LOW\_K reference at  $x=1500\text{m}$ ,  $z=0.5\text{m}$ , and  $t=130\text{h}$  (see also Figure 4). Red line shows the Gaussian distribution with the mean and variance sampled by the ensemble. (b) same as (a) but at  $x=2500\text{m}$ ,  $z=0.5\text{m}$ , and  $t=130\text{h}$ . (c) same as (a) but for the HIGH\_K reference. (d) same as (c) but at  $x=2500\text{m}$ ,  $z=0.5\text{m}$ , and  $t=130\text{h}$ .



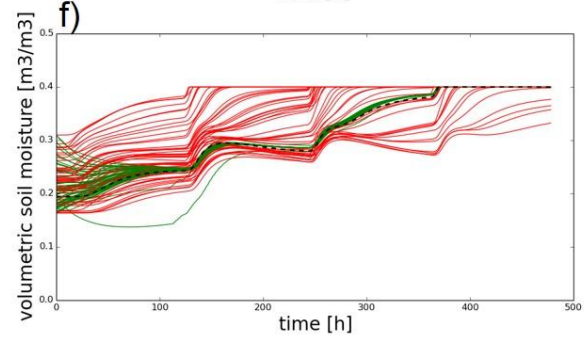
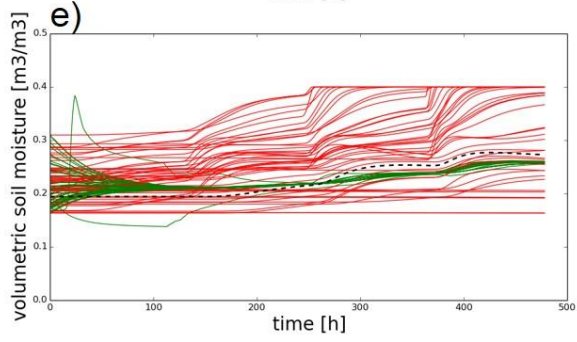
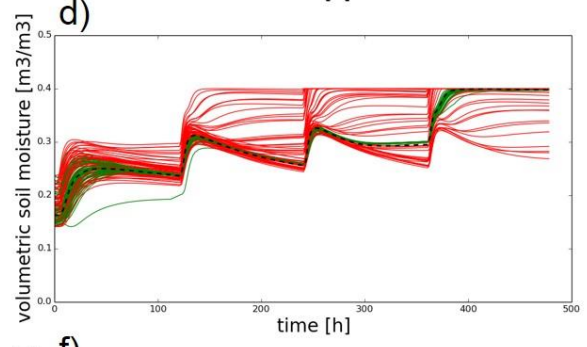
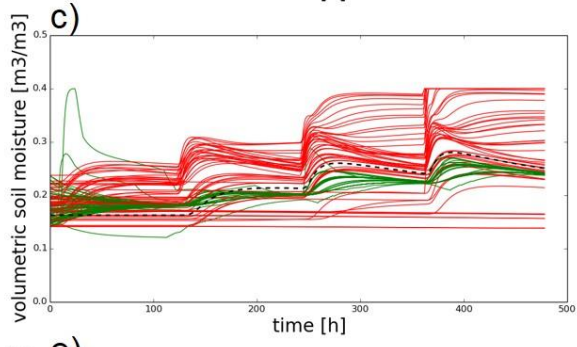
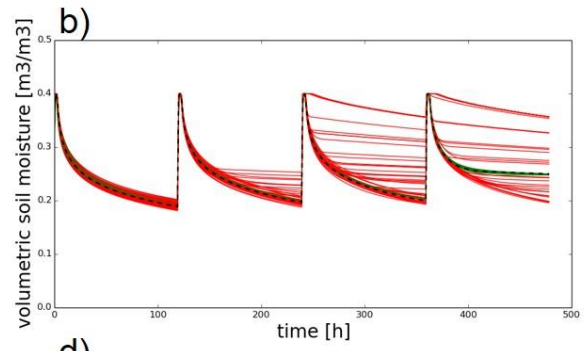
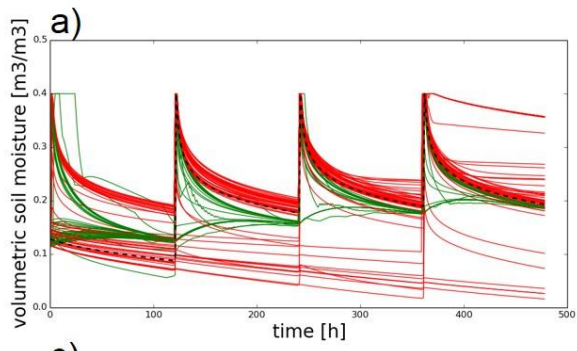
787  
788  
789  
790  
791  
792

**Figure S1.** Time series of volumetric soil moisture simulated by the synthetic reference run (black dashed line), the NoDA experiment (red lines), and the DA experiment (green lines) in the LOW\_K-UP\_O experiment at a)  $x=1500\text{m}$ ,  $z=0.05\text{m}$ ; b)  $x=2500\text{m}$ ,  $z=0.05\text{m}$ ; c)  $x=1500\text{m}$ ,  $z=1.0\text{m}$ ; d)  $x=2500\text{m}$ ,  $z=1.0\text{m}$ ; e)  $x=1500\text{m}$ ,  $z=1.5\text{m}$ ; f)  $x=2500\text{m}$ ,  $z=1.5\text{m}$ .



793  
 794  
 795

**Figure S2.** Same as Figure S1 but for the LOW\_K-DOWN\_O experiment.

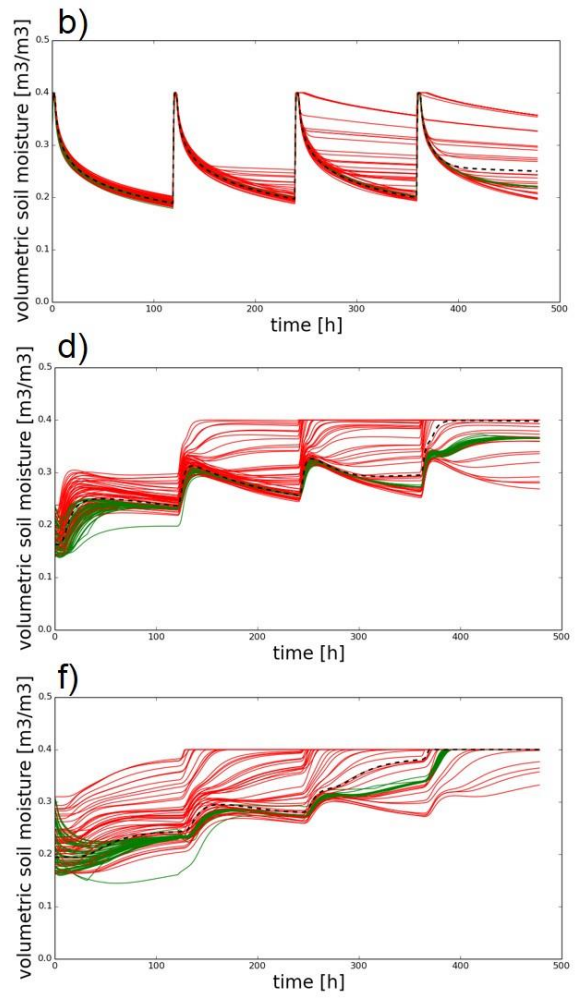
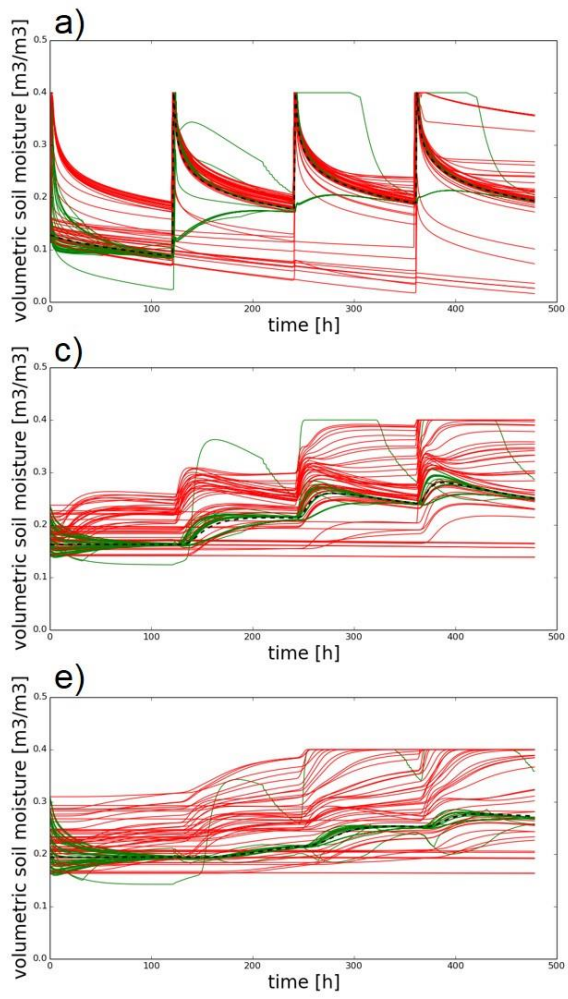


796

797

**Figure S3.** Same as Figure S1 but for the HIGH\_K-UP\_O experiment.

798



799  
800  
801

**Figure S4.** Same as Figure S1 but for the HIGH\_K-DOWN\_O experiment.